molecules

MDPI

Article

Reversible Luminescent Switching Induced by Heat/Water Treatment in a Zero-Dimensional Hybrid Antimony(III) Chloride

Ying-Chen Peng [1,†], Hao-Wei Lin [1,2,†], Sheng-Hua Zhou [1,†], Jian-Ce Jin [1], Ting-Hui Zhuang [1,3], Abdusalam Ablez [1,2], Ze-Ping Wang [1], Ke-Zhao Du [3] and Xiao-Ying Huang [1,*]

[1] State Key Laboratory of Structural Chemistry, Fujian Institute of Research on the Structure of Matter, Chinese Academy of Sciences, Fuzhou 350002, China
[2] College of Chemistry, Fuzhou University, Fuzhou 350116, China
[3] Fujian Provincial Key Laboratory of Advanced Materials Oriented Chemical Engineering, Fujian Normal University, Fuzhou 350007, China
* Correspondence: xyhuang@fjirsm.ac.cn; Fax: +86-591-6317-3145
† These authors contributed equally to this work.

Abstract: Recently zero-dimensional (0-D) inorganic–organic metal halides (IOMHs) have become a promising class of optoelectronic materials. Herein, we report a new photoluminescent (PL) 0-D antimony(III)-based IOMH single crystal, namely $[H_2BPZ][SbCl_5]\cdot H_2O$ (BPZ = benzylpiperazine). Photophysical characterizations indicate that $[H_2BPZ][SbCl_5]\cdot H_2O$ exhibits singlet/triplet dual-band emission. Density functional theory (DFT) calculations suggest that $[H_2BPZ][SbCl_5]\cdot H_2O$ has the large energy difference between singlet and triplet states, which might induce the dual emission in this compound. Temperature-dependent PL spectra analyses suggest the soft lattice and strong electron–phonon coupling in this compound. Thermogravimetric analysis shows that the water molecules in the lattice of the title crystal could be removed by thermal treatment, giving rise to a dehydrated phase of $[H_2BPZ][SbCl_5]$. Interestingly, such structural transformation is accompanied by a reversible PL emission transition between red light (630 nm, dehydrated phase) and yellow light (595 nm, water-containing phase). When being exposed to an environment with 77% relative humidity, the emission color of the dehydrated phase was able to change from red to yellow within 20 s, and the red emission could be restored after reheating. The red to yellow emission switching could be achieved in acetone with water concentration as low as 0.2 vol%. The reversible PL transition phenomenon makes $[H_2BPZ][SbCl_5]\cdot H_2O$ a potential material for luminescent water-sensing.

Keywords: inorganic–organic hybrid material; antimony halide; luminescent switching; photoluminescence; water-sensing

Citation: Peng, Y.-C.; Lin, H.-W.; Zhou, S.-H.; Jin, J.-C.; Zhuang, T.-H.; Ablez, A.; Wang, Z.-P.; Du, K.-Z.; Huang, X.-Y. Reversible Luminescent Switching Induced by Heat/Water Treatment in a Zero-Dimensional Hybrid Antimony(III) Chloride. *Molecules* **2023**, *28*, 1978. https://doi.org/10.3390/molecules28041978

Academic Editors: Xujun Zheng and Wencheng Zhu

Received: 29 January 2023
Revised: 15 February 2023
Accepted: 17 February 2023
Published: 19 February 2023

1. Introduction

Inorganic–organic metal halides (IOMHs) have drawn enormous research attention due to their outstanding optoelectronic properties of high carrier mobility, strong absorption, long carrier diffusion length, and so on [1,2]. These properties are intensively related with their delocalized electrons with large Wannier-type excitations characterized by small binding energies (10–40 meV) [3,4]. Devious choices of organic and inorganic components have made dimensional-reduced IOMHs available, which can exhibit strong structural distortions and significant quantum confinement effects [5–7]. Especially, zero-dimensional (0-D) IOMHs show localized structures, bringing faster formation and radiative recombination of excitations, which is beneficial to efficient photoluminescence (PL) [8,9]. In addition, 0-D IOMHs may own soft lattice and strong electron–phonon coupling, thus leading to interesting photoluminescent properties, including broad emission and large Stokes shift [10]. As a result, the applications of photoluminescent 0-D IOMHs have flourished in light-emitting diode [11–15], X-ray scintillator [16–18], remote thermography [19,20], optical waveguide [21], anti-counterfeiting [22–26], as well as sensor [27–30].

Previous works indicate that the PL performances (e.g., emission color, quantum yield) of 0-D IOMHs could be adjusted by supramolecular interactions induced by solvent molecules [17,31,32]. The information can be converted to visible color or optical signals [33], termed as vapochromism, which can be directly discerned by the naked eye [34]. Since the water molecule is always present in environments, such as the atmosphere, the water-molecule-sensing is of vital importance for meteorology, industrial production and human health [35–38]. Today's sensors for humidity detection include fiber optic [39], fluorescence [40], quartz crystal microbalance (QCM) [41], and capacitive and resistive ones [42]. Optical-based humidity sensors usually have better sensitivity and can be used in environments with strong electromagnetic interference [43]. Thus far, the water-induced PL vapochromism has been occasionally investigated in 0-D IOMHs. For instance, Tang's group reports on a 0-D IOMH of PEA_2MnBr_4 (PEA = doubly-protonated phenethylamine) that exhibits PL color change from green to pink at 38% relative humidity (RH) [28]; Kuang's group reports on a 0-D $(PPZ)_2SbCl_7{\cdot}5H_2O$ (PPZ = doubly-protonated 1-phenylpiperazine) with broad red emission, which could be turned to a yellow-emissive phase by removing water molecules in the crystal lattice and the water-free phase shows a water detecting limit of 1.5 vol% [30]. However, it is still challenging to realize the fast-detecting and lower-detecting limit for water-sensing by IOMHs. Herein, we synthesized a new type of water-containing metal halide single crystal, namely $[H_2BPZ][SbCl_5]{\cdot}H_2O$ (BPZ = benzylpiperazine). This 0-D antimony(III)-based IOMH exhibits yellow and red emission, respectively, during water insertion and removal. The PL switching can be as fast as 20 s, making the water detection possible.

2. Results and Discussion

2.1. Crystal Structure

The singe-crystal X-ray structure of $[H_2BPZ][SbCl_5]{\cdot}H_2O$ was determined by SCXRD at 293 K. Crystal data for $[H_2BPZ][SbCl_5]{\cdot}H_2O$ ($C_{11}H_{20}Cl_5N_2OSb$, M = 495.30 g/mol): monoclinic, space group $P2_1/c$ (no. 14), a = 15.1814(14) Å, b = 12.1122(11) Å, c = 10.4217(11) Å, β = 103.164(10)°, V = 1866.0(3) Å^3, Z = 4, T = 293(2) K, μ(Mo K_α) = 8.137 mm^{-1}, $D_{calc.}$ = 1.763 g/cm^3, 4789 reflections measured (5.108° ≤ 2θ ≤ 52.254°), 4789 unique (R_{int} = 0.0641, R_{sigma} = 0.0941) were used in all calculations (Table S1). The final R_1 was 0.0411 ($I > 2\sigma(I)$), and wR_2 was 0.0777 (all data). There is one formular unit in the asymmetric unit (Figure S1); that is, it consists of one $[H_2BPZ]^{2+}$ cation (Figure 1a), one $[SbCl_5]^{2-}$ anion (Figure 1b), and one water molecule. The inorganic $[SbCl_5]^{2-}$ anions are separated and charge-balanced by organic $[H_2BPZ]^{2+}$ cations, forming a 0-D hybrid crystal structure (Figure 1c). In the pyramid-like inorganic anionic unit, the lengths of Sb−Cl bonds range from 2.3823(11) to 2.8865(13) Å, and the angles of Cl−Sb−Cl range from 84.20(4)° to 91.60(5)° (Table 1), which are comparable to those in the literature [44]. Notably, there are abundant H-bonds (N−H···Cl and C−H···Cl H-bonds) among cations and anions, as listed in Table 2, which form a supramolecular layer structure, as shown in Figure 1d and Figure S2, where the lattice water molecules are located and form additional hydrogen bonds with Cl^- ions of the anions within the layer (Table 2). As shown in Figure 1e, the anions-packing adopts a topology of *pcu* (primitive cubic net) with a little distortion because of the low symmetry of structure and the distortion of the $[SbCl_5]^{2-}$ polyhedrons. Noteworthy is that the water molecules are located around the center of cubes built by eight $[SbCl_5]^{2-}$ units in the topology framework (Figure 1e).

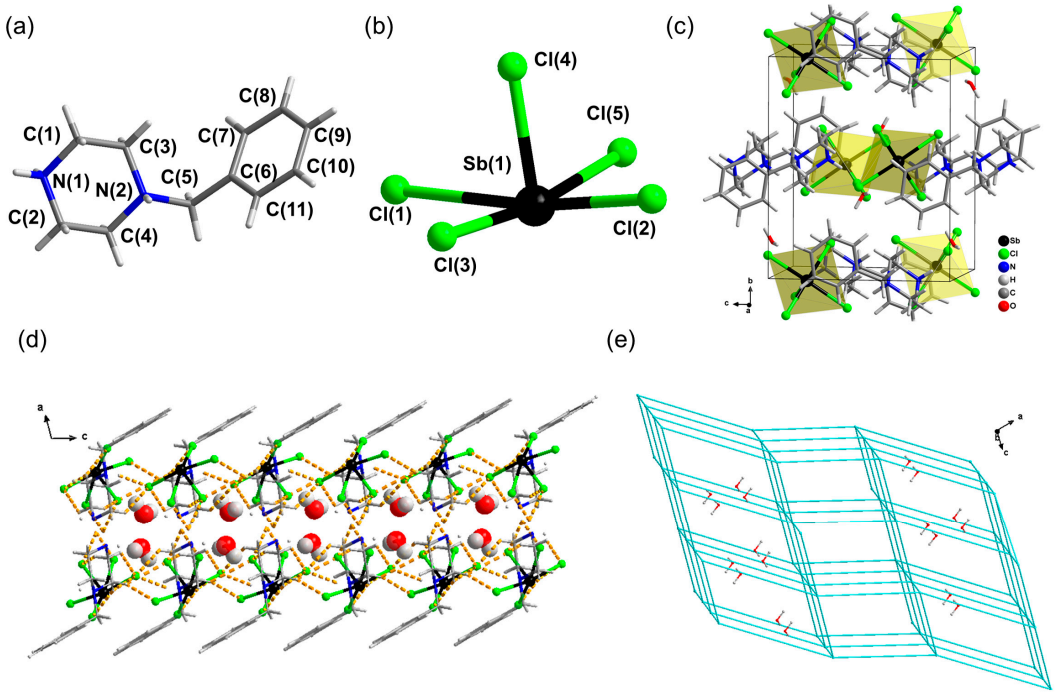

Figure 1. Structural diagrams for the title crystal $[H_2BPZ][SbCl_5]\cdot H_2O$. A $[H_2BPZ]^{2+}$ cation (**a**) and a $[SbCl_5]^{2-}$ anion (**b**) in $[H_2BPZ][SbCl_5]\cdot H_2O$. (**c**) Unit-cell-packing diagram viewed down the *a*-axis. (**d**) A supramolecular layer in $[H_2BPZ][SbCl_5]\cdot H_2O$ viewed along the *b*-axis in which lattice water molecules are located; water molecules are in CPK mode; hydrogen bonds with water molecules are not shown for clarity. (**e**) Topological net of *pcu* type for anions arrangement in $[H_2BPZ][SbCl_5]\cdot H_2O$ where the lattice water molecules are shown.

Table 1. Select bond lengths (Å) and bond angles (°) for $[H_2BPZ][SbCl_5]\cdot H_2O$ at 293 K.

Sb(1)-Cl(4)	2.3823(11)	Sb(1)-Cl(5)	2.6675(13)
Sb(1)-Cl(2)	2.4585(12)	Sb(1)-Cl(1)	2.8865(13)
Sb(1)-Cl(3)	2.5478(14)		
Cl(4)-Sb(1)-Cl(2)	88.39(4)	Cl(2)-Sb(1)-Cl(5)	90.78(5)
Cl(4)-Sb(1)-Cl(3)	88.05(4)	Cl(4)-Sb(1)-Cl(1)	83.65(4)
Cl(2)-Sb(1)-Cl(3)	91.60(5)	Cl(3)-Sb(1)-Cl(1)	88.93(5)
Cl(4)-Sb(1)-Cl(5)	84.20(4)	Cl(5)-Sb(1)-Cl(1)	87.63(4)

Symmetry transformations used to generate equivalent atoms: *n/a*.

Table 2. Hydrogen bonds for $[H_2BPZ][SbCl_5]\cdot H_2O$ at 293 K.

D-H···A	*d*(D-H)	*d*(H···A)	*d*(D···A)	<(DHA)
N(1)-H(1B)···Cl(1)	0.89	2.38	3.184(4)	151.0
N(1)-H(1B)···Cl(4)	0.89	2.67	3.210(4)	120.1
N(1)-H(1A)···O(1)	0.89	1.98	2.843(5)	163.8
N(2)-H(2)···Cl(5)#1	0.98	2.14	3.106(4)	166.9
C(1)-H(1C)···Cl(5)#1	0.97	2.90	3.632(5)	133.0
C(2)-H(2A)···Cl(5)#2	0.97	2.88	3.463(5)	119.6
C(2)-H(2B)···Cl(4)#2	0.97	2.98	3.748(4)	136.6
C(4)-H(4B)···Cl(3)#3	0.97	2.79	3.703(5)	158.0
C(4)-H(4B)···Cl(4)#3	0.97	2.91	3.594(5)	128.0
C(4)-H(4A)···Cl(2)#2	0.97	2.83	3.690(5)	148.3
C(4)-H(4A)···Cl(5)#2	0.97	2.81	3.463(4)	125.2
O(1)-H(1E)···Cl(3)#3	0.818(10)	2.67(3)	3.408(4)	152(6)
O(1)-H(1F)···Cl(1)#4	0.820(10)	2.393(12)	3.210(4)	175(6)

Symmetry transformations used to generate equivalent atoms: #1 $-x+1, -y+1, -z$ #2 $-x+1, y-1/2, -z+1/2$ #3 $-x+1, -y+1, -z+1$ #4 $-x+1, y+1/2, -z+1/2$.

In previous reports, it was found that ionic metal halide crystals could be formed by combining penta-coordinated antimony halide units of $[SbCl_5]^{2-}$ with monoprotonated 4-benzylpiperidine cations (bpzpipn), a cation with a similar structural geometry but different charge with doubly protonated benzylpiperazine of $[H_2BPZ]^{2-}$ in $[H_2BPZ][SbCl_5]\cdot H_2O$. The obtained compounds ($[bzpipn]_2SbCl_5$ [45] and $[bzpipn]_2SbCl_5\cdot H_2O$ [46]) both feature a pseudo 1D chain-like structure of $[SbCl_5]_n$ due to the presence of an additional secondary Sb···Cl bond in between adjacent $[SbCl_5]$ units with bond lengths ranging from 3.2182 to 3.3028 Å. By contrast, in the title $[H_2BPZ][SbCl_5]\cdot H_2O$, all the $[SbCl_5]$ units are discrete with a shortest Sb···Sb distance of 7.605 Å. The difference in the arrangements of $[SbCl_5]$ units in these compounds is probably related to the ability of cations of forming N−H···Cl H-bonds; note that $[H_2BPZ]$ contains a NH_2 and a NH in the piperazine ring, while [bzpipn] contains a NH_2 group only in the piperidine ring. Thus, the structural comparison made here highlights the importance of organic cations in constructing ionic metal halides with desired structure and property.

2.2. Photophysical Properties

To characterize the optical properties of $[H_2BPZ][SbCl_5]\cdot H_2O$, the steady-state and time-resolved PL spectra were measured. The steady-state PL excitation spectrum (emission = 595 nm) shows two peaks at about 265 nm and 320 nm, suggesting $^1S_0 \rightarrow {}^1P_1$ and $^1S_0 \rightarrow {}^3P_1$ electronic transitions in Sb^{3+} ions, respectively (Figure 2a) [47]. The $^1S_0 \rightarrow {}^1P_1$ electronic transition is allowed, while the $^1S_0 \rightarrow {}^3P_1$ is partially allowed by the spin–orbit coupling [48,49]. However, the steady-state PL excitation spectrum (emission = 450 nm) only shows one peak at around 275 nm, suggesting that the $^1S_0 \rightarrow {}^3P_1$ electronic transition nearly disappeared. Under the excitation of 290 nm, $[H_2BPZ][SbCl_5]\cdot H_2O$ exhibits dual-band broad emission peaking at 450 and 595 nm. The dual-band emission could be attributed to the exciton relaxation of $^1P_1 \rightarrow {}^1S_0$ and $^3P_n \rightarrow {}^1S_0$, respectively (Figure 2b). However, there is only one broad mono-band yellow emission under the excitation of 320 nm (Figure 2b); this triplet emission shows a peak centered at 595 nm with a Stokes shift of 275 nm. The title compound delivers a PLQY value of 14.33%, which is moderate among this class of compounds [26,30,31,49]. The time-resolved PL spectrum is shown in Figure 2c and utilized to calculate the PL lifetime of the title compound (Figure 2c). The lifetime of $[H_2BPZ][SbCl_5]\cdot H_2O$ can be fitted well via the biexponential function (Equation (1)) [50]:

$$I = A_1 \exp(-t/\tau_1) + A_2 \exp(-t/\tau_2) \quad (1)$$

The average lifetime can be calculated and obtained by the following Equation (2) [51]:

$$\tau_{av} = \left(A_1{\tau_1}^2 + A_2{\tau_2}^2\right)/\left(A_1\tau_1 + A_2\tau_{12}\right) \quad (2)$$

The lifetime of $[H_2BPZ][SbCl_5]\cdot H_2O$ can be fitted as 1.66 μs, which confirms the triplet emission.

After analyzing the steady-state and time-resolved PL spectra of the title compound, the PL mechanism is proposed as shown in Figure 2d [40]. Under excitation, the electrons in ground state $^1S_0$ orbitals are excited to the singlet excited state $^1P_1$ and triplet excited state ^3P_n orbitals. The intersystem crossing (ISC) from the singlet to triplet orbitals results in the strong triplet emission during the electronic relaxation.

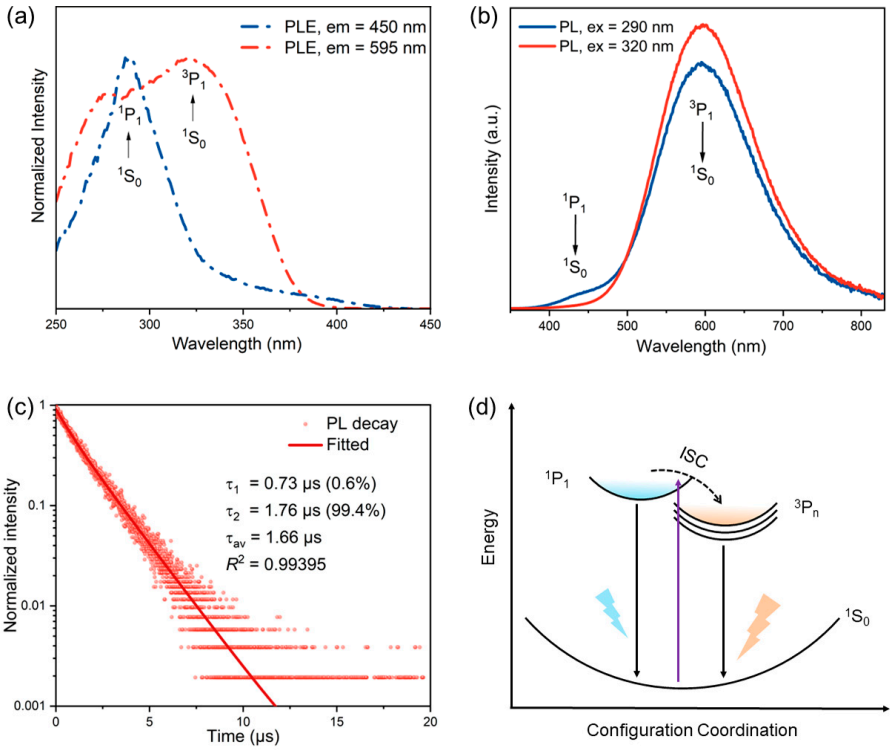

Figure 2. Steady-state and time-resolved PL spectra of $[H_2BPZ][SbCl_5]\cdot H_2O$ at RT. (**a**) The steady-state PLE spectra of $[H_2BPZ][SbCl_5]\cdot H_2O$, measured with emission wavelengths at 450 and 595 nm, respectively. (**b**) The steady-state PL spectra of $[H_2BPZ][SbCl_5]\cdot H_2O$ with excitation wavelengths at 290 and 320 nm, respectively. (**c**) Time-resolved PL spectrum of $[H_2BPZ][SbCl_5]\cdot H_2O$ at 595 nm emission. The PL lifetime is fitted, calculated, and labelled. (**d**) The proposed PL mechanism in the configuration coordinate diagram.

Furthermore, to explore the origin of the broad emission and large Stokes shift of the title compound, temperature-dependent PL spectra ranging from 80 K to 320 K were collected under an excitation of 320 nm. As shown in Figure 3a, b, the title compound shows weaker PL intensity and broadening of the emission band along with the increasing temperature. These temperature-dependent performances are comprehensible. Typically, with increasing temperature, there is enhancement of thermal vibrations resulting in a thermal quenching of PL. Whereafter, the temperature-dependent PL spectra under the 320 nm excitation are further analyzed to obtain several important physical parameters, including Huang–Rhys factor (S) and electron–phonon coupling energy (Γ_{op}). The S can be obtained by fitting the curve of FWHM vs. T using the following formula (Equation (3)):

$$\mathrm{FWHM} = 2.36\sqrt{S}\hbar\omega\sqrt{\coth\left(\frac{\hbar\omega}{2kT}\right)} \quad (3)$$

where FWHM represents full width at half maximum, $\hbar$ is Planck constant, ω is the phonon frequency, k is the Boltzmann constant, and T is temperature [52]. The S is fitted as 31.70 for $[H_2BPZ][SbCl_5]\cdot H_2O$ (Figure 3c), which is much higher than that of $CsPbBr_3$ (S = 3.22) [53] and a little higher than that of $[PPh_3H]_2[SbCl_5]$ (S = 26.91; PPh_3 = triphenylphosphine) [49], S represents the hardness or softness of the crystal lattice. A small S value represents a hard crystal lattice, which is unfavorable for electron–phonon coupling under excitation [53].

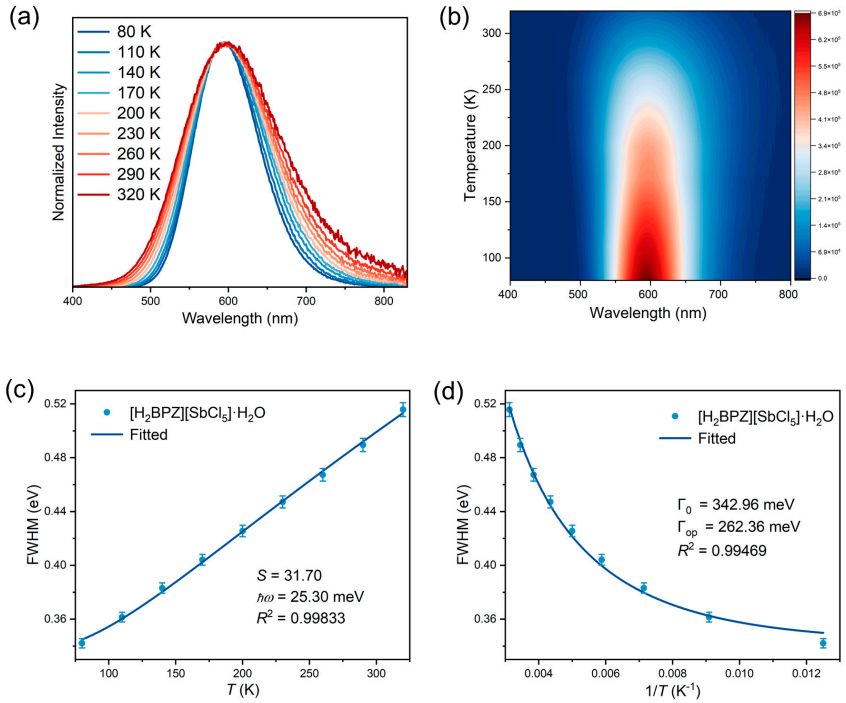

Figure 3. Temperature-dependent PL spectra and fitted physical parameters. Temperature-dependent PL spectra (**a**) and contour map (**b**) of $[H_2BPZ][SbCl_5]\cdot H_2O$ under the excitation of 320 nm. (**c**) Full width at half maximum (FWHM) vs. temperature (T) fitted by Equation (3). (**d**) FWHM vs. $1/T$ fitted by Equation (4).

To further discuss electron–phonon coupling interactions, the Toyokawa equation (Equation (4)) is used to fit the temperature-dependent PL FWHM:

$$\Gamma(T) = \Gamma_0 + \frac{\Gamma_{op}}{e^{\hbar\omega/kT}-1} \quad (4)$$

where Γ_0 represents the intrinsic line width at absolute 0 K (replaced by the data at 80 K in this work), and Γ_{op} is the electron–phonon coupling energy [54]. The Γ_{op} is fitted as 262.36 meV, larger than that of $[DMPZ]_2SbCl_6\cdot Cl\cdot(H_2O)_2$ (DMPZ = doubly protonated *N*, *N*′-dimethylpiperazine; Γ_{op} = 65.65 meV) [14] and $[PPh_3H]_2[SbCl_5]$ (Γ_{op} = 144.72 meV) [49], indicating strong electron–phonon coupling in the title compound under the excitation (Figure 3d). Overall, the temperature-dependent PL spectra analysis suggests the soft lattice and strong electron–phonon coupling in the title compound.

2.3. Theortical Calculations

Density functional theory (DFT) calculations were performed to investigate the band structure and photoluminescent mechanism of $[H_2BPZ][SbCl_5]\cdot H_2O$. As shown in Figure S5, the title compound shows a calculated direct band gap of 3.45 eV, which is very close to the experimental one of 3.25 eV (Figures S3 and S4). The DOS shows that the valence-band maximum (VBM) is mainly contributed by Sb 5*s* and Cl 3*p* and the conduction-band minimum (CBM) is mostly contributed by Sb 5*p*, C 3*s* and 3*p* (Figure 4a). The nearly dispersionless VBM indicates negligible electronic coupling between inorganic $[SbCl_5]^{2-}$ units; that is, the title compound behaves a localized electronic structure [55]. Accordingly, the highest occupied molecular orbital (HOMO) is occupied by the inorganic moiety of $[SbCl_5]^{2-}$ mostly. The electronic cloud was round-like referring to the *s* electrons for Sb atom and spindle-like referring to the p electrons for Cl atom (Figure 4b). The lowest occupied molecular orbital (LUMO) is occupied by Sb atoms and conjugate electrons in benzene rings in organic $[H_2BPZ]^{2+}$ cations (Figure 4c). The spindle-like electronic cloud of

p electrons of Sb atoms is clear. These results suggest the large energy difference between singlet and triplet states, which might induce the dual emission in the title compound [56].

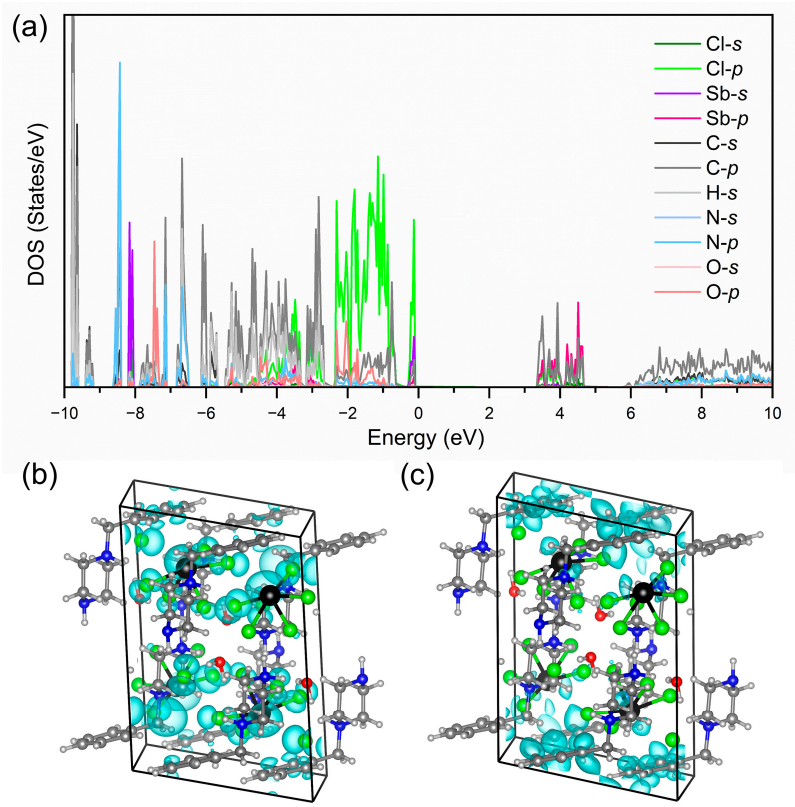

Figure 4. (**a**) The calculated orbital-resolved DOSs of $[H_2BPZ][SbCl_5]\cdot H_2O$. The highest occupied molecular orbital (HOMO; (**b**)) and lowest occupied molecular orbital (LUMO; (**c**)) along the *ac* plane of $[H_2BPZ][SbCl_5]\cdot H_2O$.

2.4. Powder X-ray Diffraction and Thermogravimetric Analysis

The purity and the stability of the title compound were measured by powder X-ray diffraction (PXRD) and thermogravimetric (TG) analysis, as shown in Figure 5. The experimental PXRD pattern of the $[H_2BPZ][SbCl_5]\cdot H_2O$ powders obtained by grinding the crystals is in agreement with the simulated one (Figure 5a), suggesting the purity and uniformity of the as-synthesized sample. Of note is that the as-synthesized crystals of $[H_2BPZ][SbCl_5]\cdot H_2O$ could be steadily stored under ambient conditions for a long time (e.g., one month), as verified by PXRD (Figure 5a). The result implies that the water molecular is stable in the crystal lattice and no phase-transition would happen at ambient conditions. The moderate steric hindrance of organic cations can construct a 2D supramolecular framework, which endows $[H_2BPZ][SbCl_5]\cdot H_2O$ with superior stability. TG analysis indicates a two-step decomposition from RT to 800 °C for $[H_2BPZ][SbCl_5]\cdot H_2O$. The first weight loss is shown in about 60 to 90 °C (experimental: 3.59% vs. theoretical: 3.64%), implying the removal of one water molecule per formula for $[H_2BPZ][SbCl_5]\cdot H_2O$ (Figure 5b). That means the chemical formula is $[H_2BPZ][SbCl_5]$ for the dehydrated phase. However, the corresponding PXRD pattern after losing water molecules differs considerably from the one of the pristine and the simulated one (Figure S6), implying a slightly changed ionic structure after the loss of water molecules [24]. The second weight loss from 90 to 340 °C corresponds to a total decomposition of the title compound.

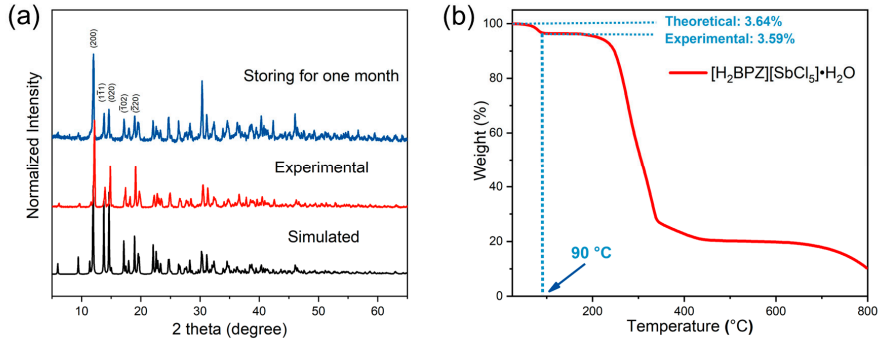

Figure 5. (**a**) The experimental PXRD patterns for as-made $[H_2BPZ][SbCl_5]\cdot H_2O$ and that storing at ambient conditions for one month compared with the one simulated from SCXRD data. (**b**) The TG curve for $[H_2BPZ][SbCl_5]\cdot H_2O$; the theoretical and experimental weight losses of water molecules in the crystal lattice were calculated and labelled.

2.5. Luminescent Water-Sensing

The water molecules could be removed by heat treatment of the title compound according to the TG analysis (Figure 5b). Thus, we have performed the dehydration of the title compound by heating at 100 °C for 30 min. After dehydration, the single crystals show pulverization and are not transparent anymore. Moreover, the PL emission has been changed from yellow to red. Interestingly, the PL of the dehydrated sample could be recovered in ambient conditions (average 21 °C and 77% humidity in Fuzhou, China) quickly (inset of Figure 6a). To further characterize the PL emission switching, in situ PL spectra were performed for the dehydrated $[H_2BPZ][SbCl_5]$ at ambient conditions. As shown in Figure 6a, the dehydrated $[H_2BPZ][SbCl_5]$ exhibits an emission peak at around 630 nm, while the emission peak shows a blue shift becoming 595 nm after 20 s. In addition, the dehydrated $[H_2BPZ][SbCl_5]$ exhibits stronger PL intensity than $[H_2BPZ][SbCl_5]\cdot H_2O$. Quick and distinct PL emission switching make luminescent water-sensing application possible. Then, we have utilized the dehydrated $[H_2BPZ][SbCl_5]$ to trace the water content in an organic solvent. Here, the dehydrated powder was soaked into acetone with different water contents (From 0–0.4% v/v). As the water concentration increased from 0.1 vol% to 0.2 vol%, the red-emissive compound turned to emit yellow light. The results show a detection limit of ca. 0.2 vol% for luminescent humidity-sensing for $[H_2BPZ][SbCl_5]$, which is lower than that of another 0-D Sb^{3+}-based IOMH of $(PPZ)_2SbCl_7\cdot 5H_2O$ (1.5 vol%) [30].

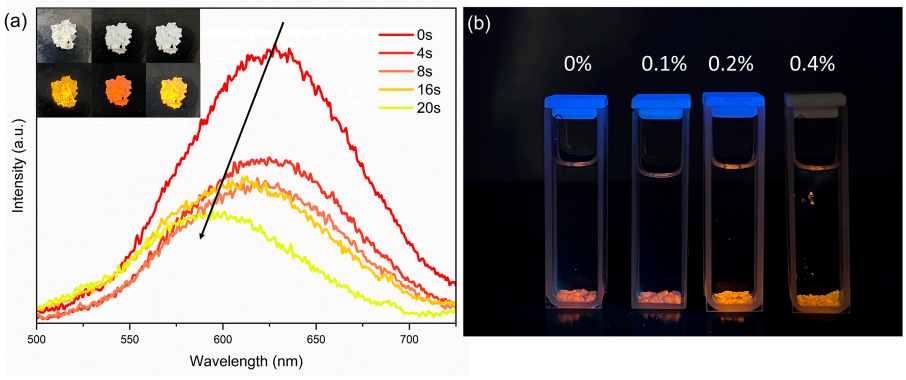

Figure 6. (**a**) The in situ PL spectra for humidity-sensing application; the red-emissive $[H_2BPZ][SbCl_5]$ can be transformed to yellow-emissive $[H_2BPZ][SbCl_5]\cdot H_2O$ within 20 s under the ambient condition. Inset: the photographs of $[H_2BPZ][SbCl_5]\cdot H_2O$ power under ambient light (top) and UV light (bottom); from left to right: freshly prepared crystals, samples after heating at 100 °C for 30 min, dehydrated samples placed in ambient condition. (**b**) Dehydrated $[H_2BPZ][SbCl_5]$ in acetone solvent containing different amounts of water (0–0.4% v/v).

3. Materials and Methods

Reagents: Antimony(III) oxide (Sb_2O_3, RG) was purchased from Adamas Reagent Co. Ltd. (Shanghai, China) Benzylpiperazine (BPZ, 99%) was purchased from J&K Scientific Reagent Co., Ltd. (Beijing, China) Hydrochloric acid solution (HCl, 37%) was purchased from Sinopharm Chemical Reagent Co., Ltd. (Shanghai, China). All reagents and solvents were used without further purification.

Synthesis of $[H_2BPZ][SbCl_5]\cdot H_2O$: 1.0 mmol Sb_2O_3 (0.2195 g), 2 mmol BPZ (0.3452 g) and 3 mL HCl (37%) were mixed in a 28 mL Teflon-lined steel autoclave. Then, the reactor was heated at 120 °C for 3 days and naturally cooled to ambient temperature in 5 h. The colorless transparent liquid was obtained and then transported into a 20 mL glass bottle. Finally, transparent colorless prismatic crystals of $[H_2BPZ][SbCl_5]\cdot H_2O$ were crystallized overnight. The product yield was 0.3616 g (73% based on Sb).

Single-Crystal X-Ray Diffraction (SCXRD): A suitable single crystal was selected under an optical microscope for SCXRD measurement. Intensity data were collected on a Supernova CCD diffractometer using graphite-monochromated Mo K_α radiation (λ = 0.71073 Å) at 293 K. The structure was solved by direct methods and refined by full-matrix least-squares on F^2 using the SHELX-2018 program package [57]. The non-hydrogen atoms were refined anisotropically. The hydrogen atoms in the $[H_2BPZ]^{2+}$ cations were located at geometrically calculated positions, while those of the lattice water molecule were located from difference-Fourier maps and their atomic positions were refined. The crystallographic data and details for structural refinements are listed in Table S1. Selected bond lengths and angles are listed in Table 1. The hydrogen-bonding data are listed in Table 2. CCDC No. 2220612 contains the supplementary crystallographic data for this paper. The data can be obtained free of charge from The Cambridge Crystallographic Data Centre via www.ccdc.cam.ac.uk/data_request/cif (accessed on 18 November 2022).

Fourier Infrared Spectroscopy (FTIR): FTIR spectrum was measured by an instrument of Vertex 70 FTIR. Detailed data are shown in Figure S7.

Powder X-Ray Diffraction (PXRD): The experimental PXRD patterns were measured by a Rigaku Miniflex-II diffractometer by utilizing Cu K_α radiation (λ = 1.54178 Å) at 30 KV and 15 mA in the angular range of 2θ = 5–65°. The experimental PXRD pattern after the loss of water molecules were measured by the X-ray diffractometer with D8 Advance made by Bruker at 40 KV and 40 mA in the angular range of 2θ = 5–65°. The simulated PXRD pattern was calculated using the SCXRD data via Mercury software.

Thermogravimetric Analysis (TGA): TG curve was recorded on a NETZSCH STA 449F3 instrument with a heating rate of 10 K min^{-1} under a dry N_2 atmosphere.

Solid-State UV-Visible Absorption Spectroscopy (UV-vis): The solid-state diffuse reflectance data were recorded on a Shimadzu 2600 UV-vis spectrometer at room temperature (RT) in the range of 800–200 nm. The $BaSO_4$ plate was utilized as a standard that possesses 100% reflectance. The absorption data were then obtained from the reflectance spectrum using the Kubelka–Munk function $\alpha/S = (1 - R)^2/2R$, where α refers to the absorption coefficient, S refers to the scattering coefficient and R refers to the reflectance [58]. The test was performed on the solid-state sample in polycrystalline form.

Steady-State Photoluminescence Spectra: The photoluminescence excitation (PLE), photoluminescence (PL) spectra and photoluminescent quantum yield (PLQY) were measured on the FLS1000 UV/V/NIR fluorescence spectrometer. The excitation light source is a solid picosecond diode exciter with a pulse width of 57 picoseconds. The tests were performed on solid-state samples in polycrystalline form.

Time-Resolved Photoluminescence Spectra: Time-resolved PL spectra were measured on the FLS1000 UV/V/NIR fluorescence spectrometer. The tests were performed on solid-state samples in polycrystalline form.

Temperature-Dependent Photoluminescence Spectra: Temperature-dependent PL spectra were measured on the FLS980 fluorescence spectrometer ranging from 80 K to 320 K. The tests were performed on the samples in polycrystalline form.

Density functional theory (DFT) calculations: DFT calculations were implemented in the Vienna Ab initio Simulation Package (VASP) [59–61]. A generalized gradient approximation (GGA) for the exchange-correlation term with Perdew–Burke–Ernzerhof (PBE) exchange–correlation functional was applied for the electron–electron exchange–correlation processes. The projected augmented wave (PAW) potentials were used with the valence states 2*s*, 2*p* for C and N; 3*s*, 3*p* for Cl and 5*s*, 5*p* for Sb, respectively. To ensure sufficient accuracy, the Brillouin zone was implemented by a Monkhorst–Pack k-point mesh of $3 \times 3 \times 5$, and a high cut-off energy of 500 eV for the plane wave expansion was chosen. The self-consistent field (SCF) computations were set to a convergence criterion of 1×10^{-5} eV and the force criterion was 0.02 eV/Å. The Fermi level (EF = 0 eV) was chosen as the reference of the energy.

4. Conclusions

In summary, a new PL 0-D IOMH of $[H_2BPZ][SbCl_5]\cdot H_2O$ has been studied in this work. The structure of this water-containing metal halide single crystal was determined in detail. The photophysical dynamics were investigated by temperature-dependent PL spectra and DFT calculations. The yellow emission of $[H_2BPZ][SbCl_5]\cdot H_2O$ originates from the recombination of singlet/triplet dual-band emission. DFT calculations show that the VBM and CBM are mostly located at the $[SbCl_5]^{2-}$ unit, resulting in a large energy difference between the singlet and triplet states. Several important parameters, including S Γ_{op}, have been fitted from temperature-dependent PL spectra. The results reveal that the large FWHM of PL should be owing to the soft lattice and strong electron–phonon coupling. It is worth noting that the water molecules in the $[H_2BPZ][SbCl_5]\cdot H_2O$ structure can be removed by heating, which causes the luminescent color change from yellow to red. The removed water molecules can be quickly restored to the material in the high RH environment or solution with water concentration as low as 0.2 vol%. This study not only provides a new type of lead-free metal halide-based emitter, but also paves the way for designing new PL metal halide materials for humidity-sensing.

Supplementary Materials: The following supporting information can be downloaded at: https://www.mdpi.com/article/10.3390/molecules28041978/s1. Table S1: Crystal data and structure refinement details for $[H_2BPZ][SbCl_5]\cdot H_2O$ at 293 K; Figure S1: *ORTEP* drawing (50% ellipsoid probability) of the asymmetric unit of $[H_2BPZ][SbCl_5]\cdot H_2O$ at 293 K; Figure S2: A supramolecular layer in $[H_2BPZ][SbCl_5]\cdot H_2O$ viewed along the *a*-axis in which lattice water molecules are located; water molecules are in CPK mode; hydrogen bonds with water molecules are not shown; Figure S3: Solid-state UV-visible absorption spectrum of $[H_2BPZ][SbCl_5]\cdot H_2O$ at RT; Figure S4: The experimental direct band gap of $[H_2BPZ][SbCl_5]\cdot H_2O$ calculated as 3.25 eV; Figure S5: The band structure of $[H_2BPZ][SbCl_5]\cdot H_2O$ and the direct band gap is calculated as 3.45 eV; Figure S6: The simulated (bottom) and experimental (middle) PXRD patterns for $[H_2BPZ][SbCl_5]\cdot H_2O$, and experimental PXRD pattern for $[H_2BPZ][SbCl_5]$ (top); Figure S7: FTIR spectrum of $[H_2BPZ][SbCl_5]\cdot H_2O$ crystal powder at RT.

Author Contributions: Conceptualization, Y.-C.P., Z.-P.W., K.-Z.D. and X.-Y.H.; methodology, Y.-C.P., H.-W.L., S.-H.Z., T.-H.Z., J.-C.J. and A.A.; software, Y.-C.P., S.-H.Z., H.-W.L. and X.-Y.H.; validation, Y.-C.P. and X.-Y.H.; formal analysis, Y.-C.P., H.-W.L. and S.-H.Z.; investigation, Y.-C.P. and H.-W.L.; resources, X.-Y.H.; writing—original draft preparation, Y.-C.P., Z.-P.W., S.-H.Z., K.-Z.D. and X.-Y.H.; writing—review and editing, Y.-C.P., H.-W.L., Z.-P.W., K.-Z.D. and X.-Y.H.; visualization, Y.-C.P.; supervision, X.-Y.H.; project administration, X.-Y.H.; funding acquisition, X.-Y.H. All authors have read and agreed to the published version of the manuscript.

Funding: This work was supported by the National Natural Science Foundation of China (No. 9226115) and the Natural Science Foundation of Fujian Province (No. 2020J01118).

Institutional Review Board Statement: Not applicable.

Data Availability Statement: All the available data are incorporated in the MS.

Acknowledgments: We thank Jing-Jing Fu for their help in photoluminescence characterizations.

Conflicts of Interest: The authors declare no conflict of interest.

References

1. Kojima, A.; Teshima, K.; Shirai, Y.; Miyasaka, T. Organometal halide perovskites as visible-light sensitizers for photovoltaic cells. *J. Am. Chem. Soc.* **2009**, *131*, 6050–6051. [CrossRef] [PubMed]
2. Lee, M.M.; Teuscher, J.; Miyasaka, T.; Murakami, T.N.; Snaith, H.J. Efficient hybrid solar cells based on meso-superstructured organometal halide perovskites. *Science* **2012**, *338*, 643–647. [CrossRef] [PubMed]
3. Burschka, J.; Pellet, N.; Moon, S.J.; Humphry-Baker, R.; Gao, P.; Nazeeruddin, M.K.; Gratzel, M. Sequential deposition as a route to high-performance perovskite-sensitized solar cells. *Nature* **2013**, *499*, 316–319. [CrossRef]
4. Morad, V.; Shynkarenko, Y.; Yakunin, S.; Brumberg, A.; Schaller, R.D.; Kovalenko, M.V. Disphenoidal zero-dimensional lead, tin, and germanium halides: Highly emissive singlet and triplet self-trapped excitons and X-ray scintillation. *J. Am. Chem. Soc.* **2019**, *141*, 9764–9768. [CrossRef] [PubMed]
5. Saparov, B.; Mitzi, D.B. Organic-inorganic perovskites: Structural versatility for functional materials design. *Chem. Rev.* **2016**, *116*, 4558–4596. [CrossRef]
6. Mao, L.; Stoumpos, C.C.; Kanatzidis, M.G. Two-dimensional hybrid halide perovskites: Principles and promises. *J. Am. Chem. Soc.* **2019**, *141*, 1171–1190. [CrossRef]
7. Li, X.; Hoffman, J.M.; Kanatzidis, M.G. The 2D halide perovskite rulebook: How the spacer influences everything from the structure to optoelectronic device efficiency. *Chem. Rev.* **2021**, *121*, 2230–2291. [CrossRef]
8. Jin, J.C.; Shen, N.N.; Wang, Z.P.; Peng, Y.C.; Huang, X.Y. Photoluminescent ionic metal halides based on s^2 typed ions and aprotic ionic liquid cations. *Coord. Chem. Rev.* **2021**, *448*, 41. [CrossRef]
9. Li, M.; Xia, Z. Recent progress of zero-dimensional luminescent metal halides. *Chem. Soc. Rev.* **2021**, *50*, 2626–2662. [CrossRef]
10. Li, S.; Luo, J.; Liu, J.; Tang, J. Self-trapped excitons in all-inorganic halide perovskites: Fundamentals, status, and potential applications. *J. Phys. Chem. Lett.* **2019**, *10*, 1999–2007. [CrossRef]
11. Li, J.L.; Sang, Y.F.; Xu, L.J.; Lu, H.Y.; Wang, J.Y.; Chen, Z.N. Highly efficient light-emitting diodes based on an organic antimony(III) halide hybrid. *Angew. Chem. Int. Ed.* **2022**, *61*, e202113450. [CrossRef]
12. Li, D.Y.; Sun, Y.M.; Wang, X.Y.; Wang, N.N.; Zhang, X.Y.; Yue, C.Y.; Lei, X.W. Zero-dimensional hybrid indium halides with efficient and tunable white-light emissions. *J. Phys. Chem. Lett.* **2022**, *13*, 6635–6643. [CrossRef] [PubMed]
13. Jin, J.C.; Peng, Y.H.; Xu, Y.T.; Han, K.; Zhang, A.R.; Yang, X.B.; Xia, Z.G. Bright green emission from self-trapped excitons triggered by Sb^{3+} doping in Rb_4CdCl_6. *Chem. Mater.* **2022**, *34*, 5717–5725. [CrossRef]
14. Zhao, J.Q.; Han, M.F.; Zhao, X.J.; Ma, Y.Y.; Jing, C.Q.; Pan, H.M.; Li, D.Y.; Yue, C.Y.; Lei, X.W. Structural dimensionality modulation toward enhanced photoluminescence efficiencies of hybrid lead-free antimony halides. *Adv. Opt. Mater.* **2021**, *9*, 2100556. [CrossRef]
15. Liu, H.; Shonde, T.B.; Gonzalez, F.; Olasupo, O.J.; Lee, S.; Luong, D.; Lin, X.; Vellore Winfred, J.S.R.; Lochner, E.; Fatima, I.; et al. Efficient red light emitting diodes based on a zero-dimensional organic antimony halide hybrid. *Adv. Mater.* **2022**, 2209417. [CrossRef]
16. Su, B.; Han, K.; Xia, Z. Mn^{2+}-doped Cs_2ZnBr_4 scintillator for X-ray imaging. *J. Mater. Chem. C* **2023**. [CrossRef]
17. Peng, Y.C.; Zhou, S.H.; Jin, J.C.; Gu, Q.; Zhuang, T.H.; Gong, L.K.; Wang, Z.P.; Du, K.Z.; Huang, X.Y. Nearly one-fold enhancement in photoluminescence quantum yield for isostructural zero-dimensional hybrid antimony(III) bromides by supramolecular interaction adjustments. *Dalton Trans.* **2022**, *51*, 4919–4926. [CrossRef]
18. He, Q.Q.; Zhou, C.K.; Xu, L.J.; Lee, S.J.; Lin, X.S.; Neu, J.; Worku, M.; Chaaban, M.; Ma, B.W. Highly stable organic antimony halide crystals for X-ray scintillation. *ACS Mater. Lett.* **2020**, *2*, 633–638. [CrossRef]
19. Wu, L.-K.; Sun, H.-Y.; Li, L.-H.; Li, R.-F.; Ye, H.-Y.; Li, J.-R. Te^{4+}-doping rubidium scandium halide perovskite single crystals enabling optical thermometry. *J. Phys. Chem. C* **2022**, *126*, 21689–21698. [CrossRef]
20. Morad, V.; Yakunin, S.; Benin, B.M.; Shynkarenko, Y.; Grotevent, M.J.; Shorubalko, I.; Boehme, S.C.; Kovalenko, M.V. Hybrid 0D antimony halides as air-stable luminophores for high-spatial-resolution remote thermography. *Adv. Mater.* **2021**, *33*, e2007355. [CrossRef]
21. Liu, F.; Zhang, T.; Mondal, D.; Teng, S.; Zhang, Y.; Huang, K.; Wang, D.; Yang, W.; Mahadevan, P.; Zhao, Y.S.; et al. Light-emitting metal-organic halide 1D and 2D structures: Near-unity quantum efficiency, low-loss optical waveguide and highly polarized emission. *Angew. Chem. Int. Ed.* **2021**, *60*, 13548–13553. [CrossRef]
22. Zhao, J.Q.; Shi, H.S.; Zeng, L.R.; Ge, H.; Hou, Y.H.; Wu, X.M.; Yue, C.Y.; Lei, X.W. Highly emissive zero-dimensional antimony halide for anti-counterfeiting and confidential information encryption-decryption. *Chem. Eng. J.* **2022**, *431*, 134336. [CrossRef]
23. Luo, Z.S.; Liu, Y.J.; Liu, Y.L.; Li, C.; Li, Y.W.; Li, Q.; Wei, Y.; Zhang, L.M.; Xu, B.; Chang, X.Y.; et al. Integrated afterglow and self-trapped exciton emissions in hybrid metal halides for anti-counterfeiting applications. *Adv. Mater.* **2022**, *34*, 2200607. [CrossRef]
24. Li, D.Y.; Song, J.H.; Xu, Z.Y.; Gao, Y.J.; Yin, X.; Hou, Y.H.; Feng, L.J.; Yue, C.Y.; Fei, H.H.; Lei, X.W. Reversible triple-mode switching in photoluminescence from 0D hybrid antimony halides. *Chem. Mater.* **2022**, *34*, 6985–6995. [CrossRef]

25. Fan, L.B.; Liu, K.; He, S.H.; Zhao, F.Y.; Zhao, J.; Wang, Y.G.; Liu, Q.L. Reversible mechanically induced on-off photoluminescence in hybrid metal halides. *Adv. Funct. Mater.* **2022**, *32*, 2110771. [CrossRef]
26. Zhang, Z.; Lin, Y.; Jin, J.; Gong, L.; Peng, Y.; Song, Y.; Shen, N.; Wang, Z.; Du, K.; Huang, X. Crystalline-phase-recognition-induced domino phase transition and luminescence switching for advanced information encryption. *Angew. Chem. Int. Ed.* **2021**, *60*, 23373–23379. [CrossRef] [PubMed]
27. Li, M.; Zhou, J.; Molokeev, M.S.; Jiang, X.; Lin, Z.; Zhao, J.; Xia, Z. Lead-free hybrid metal halides with a green-emissive $[MnBr_4]$ unit as a selective turn-on fluorescent sensor for acetone. *Inorg. Chem.* **2019**, *58*, 13464–13470. [CrossRef]
28. Gao, W.; Leng, M.; Hu, Z.; Li, J.; Li, D.; Liu, H.; Gao, L.; Niu, G.; Tang, J. Reversible luminescent humidity chromism of organic-inorganic hybrid PEA_2MnBr_4 single crystals. *Dalton Trans.* **2020**, *49*, 5662–5668. [CrossRef] [PubMed]
29. Li, D.Y.; Song, J.H.; Cheng, Y.; Wu, X.M.; Wang, Y.Y.; Sun, C.J.; Yue, C.Y.; Lei, X.W. Ultra-sensitive, selective and repeatable fluorescence sensor for methanol based on a highly emissive 0D hybrid lead-free perovskite. *Angew. Chem. Int. Ed.* **2022**, *61*, e202206437. [CrossRef]
30. Luo, J.B.; Wei, J.H.; Zhang, Z.Z.; Kuang, D.B. Water-molecule-induced emission transformation of zero-dimension antimony-based metal halide. *Inorg. Chem.* **2022**, *61*, 338–345. [CrossRef] [PubMed]
31. Peng, Y.C.; Jin, J.C.; Gu, Q.; Dong, Y.; Zhang, Z.Z.; Zhuang, T.H.; Gong, L.K.; Ma, W.; Wang, Z.P.; Du, K.Z.; et al. Selective luminescence response of a zero-dimensional hybrid antimony(III) halide to solvent molecules: Size-effect and supramolecular interactions. *Inorg. Chem.* **2021**, *60*, 17837–17845. [CrossRef] [PubMed]
32. Peng, Y.C.; Zhang, Z.Z.; Lin, Y.P.; Jin, J.C.; Zhuang, T.H.; Gong, L.K.; Wang, Z.P.; Du, K.Z.; Huang, X.Y. A deep-red-emission antimony(III) chloride with dual-cations: Extremely large stokes shift due to high $SbCl_6$ distortion. *Chem. Commun.* **2021**, *57*, 13784–13787. [CrossRef] [PubMed]
33. Gao, Y.J.; Romolini, G.; Huang, H.W.; Jin, H.D.; Saha, R.A.; Ghosh, B.; De Ras, M.; Wang, C.H.; Steele, J.A.; Debroye, E.; et al. Ultrasensitive turn-on luminescence humidity sensor based on a perovskite/zeolite composite. *J. Mater. Chem. C* **2022**, *10*, 12191–12196. [CrossRef]
34. Jiang, C.; Zhong, N.; Luo, C.; Lin, H.; Zhang, Y.; Peng, H.; Duan, C.G. $(Diisopropylammonium)_2MnBr_4$: A multifunctional ferroelectric with efficient green-emission and excellent gas sensing properties. *Chem. Commun.* **2017**, *53*, 5954–5957. [CrossRef] [PubMed]
35. Wang, L.; Li, Y. Luminescent coordination compound nanospheres for water determination. *Small* **2007**, *3*, 1218–1221. [CrossRef]
36. Gao, Y.; Jing, P.; Yan, N.; Hilbers, M.; Zhang, H.; Rothenberg, G.; Tanase, S. Dual-mode humidity detection using a lanthanide-based metal-organic framework: Towards multifunctional humidity sensors. *Chem. Commun.* **2017**, *53*, 4465–4468. [CrossRef]
37. Kruse, P. Review on water quality sensors. *J. Phys. D Appl. Phys.* **2018**, *51*, 203002. [CrossRef]
38. Zhai, X.Y.; Feng, P.F.; Song, N.; Zhao, G.D.; Liu, Q.Y.; Liu, L.L.; Tang, M.; Tang, Y. Dual-functional ratiometric fluorescent sensor based on mixed-lanthanide metal-organic frameworks for the detection of trace water and temperature. *Inorg. Chem. Front.* **2022**, *9*, 1406–1415. [CrossRef]
39. Fan, L.; Bao, Y. Review of fiber optic sensors for corrosion monitoring in reinforced concrete. *Cem. Concr. Compos.* **2021**, *120*, 104029. [CrossRef]
40. Wang, Z.; Huang, X. Luminescent organic-inorganic hybrid metal halides: An emerging class of stimuli-responsive materials. *Chem. Eur. J.* **2022**, *28*, e202200609. [CrossRef]
41. Fauzi, F.; Rianjanu, A.; Santoso, I.; Triyana, K. Gas and humidity sensing with quartz crystal microbalance (QCM) coated with graphene-based materials—A mini review. *Sens. Actuators A Phys.* **2021**, *330*, 112837. [CrossRef]
42. Najeeb, M.A.; Ahmad, Z.; Shakoor, R.A. Organic thin-film capacitive and resistive humidity sensors: A Focus Review. *Adv. Mater. Interfaces* **2018**, *5*, 1800969. [CrossRef]
43. Rao, X.; Zhao, L.; Xu, L.; Wang, Y.; Liu, K.; Wang, Y.; Chen, G.Y.; Liu, T.; Wang, Y. Review of optical humidity sensors. *Sensors* **2021**, *21*, 8049. [CrossRef] [PubMed]
44. Wang, Z.; Zhang, Z.; Tao, L.; Shen, N.; Hu, B.; Gong, L.; Li, J.; Chen, X.; Huang, X. Hybrid chloroantimonates(III): Thermally induced triple-mode reversible luminescent switching and laser-printable rewritable luminescent paper. *Angew. Chem. Int. Ed.* **2019**, *58*, 9974–9978. [CrossRef] [PubMed]
45. Cariati, F.; Panzanelli, A.; Antolini, L.; Menabue, L.; Pellacani, G.C.; Marcotrigiano, G. Low-frequency vibrational-spectra of some 4-benzylpiperidinium and *N*-benzylpiperazinium pentahalogenoantimonates(III) and pentahalogenobismuthates(III)—partial crystal-structure determination of 4-benzylpiperidinium pentachloroantimonate(III). *J. Chem. Soc. -Dalton Trans.* **1981**, *4*, 909–913. [CrossRef]
46. Chaabouni, S.; Savariault, J.M.; Ben Salah, A. Crystal structure of di(*N*-benzyl piperidinium) pentachloroantimonate(III) dihydrate. *J. Chem. Crystallogr.* **2004**, *34*, 223–227. [CrossRef]
47. Vogler, A.; Nikol, H. The structures of s^2-metal complexes in the ground and sp excited states. *Inorg. Chem.* **1993**, *14*, 245–261. [CrossRef]
48. Li, Z.; Li, Y.; Liang, P.; Zhou, T.; Wang, L.; Xie, R.-J. Dual-band luminescent lead-free antimony chloride halides with near-unity photoluminescence quantum efficiency. *Chem. Mater.* **2019**, *31*, 9363–9371. [CrossRef]
49. Peng, Y.-C.; Zhou, S.-H.; Jin, J.-C.; Zhuang, T.-H.; Gong, L.-K.; Lin, H.-W.; Wang, Z.-P.; Du, K.-Z.; Huang, X.-Y. $[PPh_3h]_2[SbCl_5]$: A zero-dimensional hybrid metal halide with a supramolecular framework and stable dual-band emission. *J. Phys. Chem. C* **2022**, *126*, 17381–17389. [CrossRef]

50. Boens, N.; Ameloot, M.; Yamazaki, I.; Deschryver, F.C. On the use and the performance of the delta-function convolution method for the estimation of fluorescence decay parameters. *Chem. Phys.* **1988**, *121*, 73–86. [CrossRef]
51. Zatryb, G.; Klak, M.M. On the choice of proper average lifetime formula for an ensemble of emitters showing non-single exponential photoluminescence decay. *J. Phys. -Condes. Matter* **2020**, *32*, 415902. [CrossRef]
52. Stadler, W.; Hofmann, D.M.; Alt, H.C.; Muschik, T.; Meyer, B.K. Optical investigations of defects in $Cd_{1-x}Zn_xTe$. *Phys. Rev. B* **1995**, *51*, 10619–10630. [CrossRef] [PubMed]
53. Lao, X.; Yang, Z.; Su, Z.; Bao, Y.; Zhang, J.; Wang, X.; Cui, X.; Wang, M.; Yao, X.; Xu, S. Anomalous temperature-dependent exciton–phonon coupling in cesium lead bromide perovskite nanosheets. *J. Phys. Chem. C* **2019**, *123*, 5128–5135. [CrossRef]
54. Lee, J.; Koteles, E.S.; Vassell, M.O. Luminescence linewidths of excitons in gaas quantum-wells below 150-K. *Phys. Rev. B* **1986**, *33*, 5512–5516. [CrossRef] [PubMed]
55. Han, D.; Shi, H.; Ming, W.; Zhou, C.; Ma, B.; Saparov, B.; Ma, Y.-Z.; Chen, S.; Du, M.-H. Unraveling luminescence mechanisms in zero-dimensional halide perovskites. *J. Mater. Chem. C* **2018**, *6*, 6398–6405. [CrossRef]
56. Liu, S.; Yang, B.; Chen, J.; Wei, D.; Zheng, D.; Kong, Q.; Deng, W.; Han, K. Efficient thermally activated delayed fluorescence from all-inorganic cesium zirconium halide perovskite nanocrystals. *Angew. Chem. Int. Ed.* **2020**, *59*, 21925–21929. [CrossRef]
57. Sheldrick, G.M. Crystal structure refinement with shelxl. *Acta Crystallogr. Sect. C -Struct. Chem.* **2015**, *71*, 3–8. [CrossRef] [PubMed]
58. Wendlandt, W.M.; Hecht, H.G. *Reflectance Spectroscopy*; Interscience: New York, NY, USA, 1966.
59. Kresse, G.; Furthmuller, J. Efficiency of ab-initio total energy calculations for metals and semiconductors using a plane-wave basis set. *Comput. Mater. Sci.* **1996**, *6*, 15–50. [CrossRef]
60. Perdew, J.P.; Burke, K.; Ernzerhof, M. Generalized gradient approximation made simple. *Phys. Rev. Lett.* **1996**, *77*, 3865–3868. [CrossRef]
61. Kresse, G.; Hafner, J. Ab initio molecular dynamics for liquid metals. *Phys. Rev. B Condens. Matter* **1993**, *47*, 558–561. [CrossRef]